Title

A Dense Starburst Plexus Is Critical for Generating Direction Selectivity

Journal

Current Biology, 28(8)

ISSN

0960-9822

Authors

Morrie, Ryan D
Feller, Marla B

Publication Date

2018-04-01

DOI

10.1016/j.cub.2018.03.001

Peer reviewed

HHS Public Access

Author manuscript

Curr Biol. Author manuscript; available in PMC 2019 April 23.

Published in final edited form as:

Curr Biol. 2018 April 23; 28(8): 1204–1212.e5. doi:10.1016/j.cub.2018.03.001.

A dense starburst plexus is critical for generating direction selectivity

Ryan D. Morrie[1] and **Marla B. Feller**[1,2,*]

[1]Department of Molecular and Cell Biology, University of California, Berkeley, Berkeley, CA 94720, USA

[2]Helen Wills Neuroscience Institute, University of California, Berkeley, Berkeley, CA, 94720, USA

Summary

Starburst amacrine cell (SAC) morphology is considered central to retinal direction selectivity (DS). In *Sema6A*$^{-/-}$ mice, SAC dendritic arbors are smaller and no longer radially symmetric, leading to a reduction in SAC dendritic plexus density. *Sema6A*$^{-/-}$ mice also have a dramatic reduction in the directional tuning of retinal direction-selective ganglion cells (DSGCs). Here we show that the loss of DSGC tuning in *Sema6A*$^{-/-}$ mice is due to reduced null direction inhibition, even though strong asymmetric SAC-DSGC connectivity and SAC dendritic direction selectivity are maintained. Hence, the reduced coverage factor of SAC dendrites leads specifically to a loss of null direction inhibition. Moreover, SAC dendrites are no longer strictly tuned to centrifugal motion, indicating that SAC morphology is critical in coordinating synaptic connectivity and dendritic integration to generate direction selectivity.

Graphical abstract

Morrie and Feller show that dense SAC dendritic coverage is critical for generating DSGC tuning and asymmetric SAC-DSGC connectivity is independent of distal SAC morphology. Furthermore, they show that the directional preference of SAC varicosities is determined by the local orientation of the most distal neurite segments with glutamate receptors.

*Lead contact: correspondence should be addressed to MBF (mfeller@berkeley.edu).

Author Contributions: R.D.M. conducted the experiments and analyzed data. R.D.M. and M.B.F. designed the experiments and wrote the paper.

Declaration of Interests: The authors declare no competing interests.

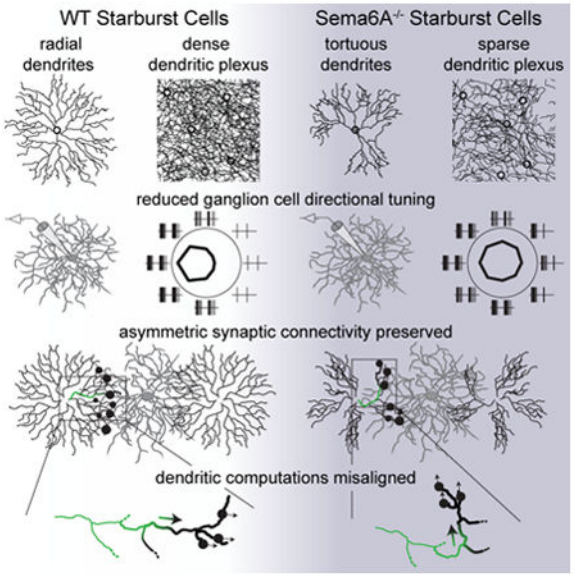

Introduction

Starburst amacrine cells (SACs) have provided a rich model to analyze the relationship between neuronal morphology and circuit computations. SACs are radially symmetric retinal interneurons whose neurites function as both dendrites and axons, with pre-synaptic release sites restricted to the distal third and post-synaptic structures to the inner two-thirds of the neurite in mice [1-3] or along the entire neurite in rabbits [4, 5]. While most retinal neuron types tile the retina, SACs neurites, which we will henceforth refer to as dendrites, overlap extensively, forming a thick plexus of highly fasiculated processes across the inner retina. Furthermore, unlike other retinal interneurons whose arbors also form a highly overlapping plexus to serve a neuromodulatory role, such as dopaminergic amacrine cells, (reviewed in [6]), SACs contribute to direction selectivity, a precise circuit computation, via several subcellular features (reviewed in [7, 8]). First, SACs synapse onto direction selective ganglion cells (DSGCs) with subcellular precision – individual SAC dendrites form GABAergic synaptic connections with DSGC subtypes when the SAC dendrite is oriented in the DSGCs' null direction [9-11]. Second, individual SAC dendrites have direction selective Ca^{2+} responses in which motion away from the soma, termed centrifugal motion, generates a larger calcium transient in the distal release sites than motion toward the soma [1, 5, 12, 13].

To what extent are these synaptic and dendritic properties dependent on the density and radial symmetry of the SAC arbor? Two gene families have been identified as critical for SAC morphology. One is the protocadherin-γ (*Pcdhg*) cluster [14]. Each SAC expresses a single protocadherin isoform, leading to homotypic dendritic self-avoidance in individual SACs but synaptic connections between different SACs [14, 15]. Deletion of the entire *Pcdhg* cluster in SACs causes a collapse of the SAC structure [14], dramatically reducing direction selectivity in DSGCs, and alters the spatial pattern of inter-SAC inhibitory synaptic signaling [15]. However, whether the absence of DSGC direction selectivity directly results

from changes in SAC-DSGC synaptic connectivity or SAC dendritic DS computations has not been explored.

A second gene family implicated in SAC dendritic development is semaphorins, a class of transmembrane proteins with multiple roles in synapse development, axon guidance, and laminar specification, especially within the retina (reviewed in [16]). Sema6A is essential for the ON/OFF segregation found in the inner plexiform layer of the retina, and signals repulsively through PlexinA2 to achieve proper lamination of ON and OFF SAC dendrites [17]. In addition, in *Sema6A*$^{-/-}$ mice, ON, but not OFF, SACs lose their radial morphological symmetry, appearing as if pie slices have been removed from their circular shape. In contrast to the *Pcdhg*$^{-/-}$ SAC phenotype, in which SAC dendrites fail to exhibit self-avoidance beginning at the soma, *Sema6A*$^{-/-}$ SAC phenotypes are milder, with SACs only failing to exhibit self-avoidance at the distal third of their dendrites [17]. Despite this more moderate phenotype in SACs, DSGCs in *Sema6A*$^{-/-}$ mice exhibit the same dramatic degree of reduced DS tuning as in *Pcdhg*$^{-/-}$ mice [15, 17].

Here, we take advantage of the altered SAC morphology in *Sema6A*$^{-/-}$ mice to determine how SAC dendritic architecture instructs synaptic wiring and subcellular computations in the direction selective circuit.

Results

DSGCs in Sema6A$^{-/-}$ mice receive weak and symmetric ON response inhibition

Sema6A is expressed in ON, but not OFF, SACs and thus the hypomorphic *Sema6A*^{lacZ} allele in the gene-trap *Sema6A*$^{-/-}$ mouse ([18], A. Kolodkin, personal communication) leads to a reduction specifically in ON SAC dendritic length and coverage, creating large gaps in the SAC plexus in the ON, but not OFF, sublamina of the IPL. These phenotypes were correlated with a significant decrease in DSGC tuning for ON, but not OFF, responses in these mice [17], but the underlying synaptic basis for this loss of direction selectivity remained unknown.

To determine whether SAC mediated inhibition onto DSGCs was affected in *Sema6A*$^{-/-}$ mice, we first performed targeted cell attached recordings from genetically identified DSGCs and stimulated them with moving bars. We observed a striking decrease in ON response direction selectivity due to an increase in null direction evoked firing (Figure 1A,B,E, Figure S1D), consistent with [17]. We then performed whole cell voltage clamp recordings from DSGCs, and observed a corresponding decrease in null direction evoked inhibition (Figure 1C,D,F) but not an increase in null direction evoked excitation (Figure S1A-C). We also observed a slight decrease in OFF direction selectivity, (Figure 1A,B, Figure S1D), but not in null direction evoked OFF inhibitory responses (Figure 1C,D, Figure S1E), indicating that the small changes in OFF spiking likely arise from the reduced laminar segregation of ON and OFF SAC dendrites in the *Sema6A*$^{-/-}$ mouse [17].

DSGCs receive inhibition from two sources – symmetric input from non-SAC GABAergic interneurons [19], and asymmetric input from SACs, in which most SAC mediated inhibition onto DSGCs occurs during null direction stimulation [20]. Therefore, we directly compared

DSGC spike tuning to the amount of asymmetric SAC mediated inhibitory input, which we estimated by computing the difference in inhibition along the nasal-temporal axis, which is the preferred-null axis for the Control GFP^{+} DSGCs in this study. We found that, regardless of genotype or luminance change direction, DSGC tuning increased with increased SAC synaptic input (Figure 1G). Overall, these results indicate that the reduction in directional tuning in DSGCs in *Sema6A*$^{-/-}$ mice is due to a loss of asymmetric SAC-mediated inhibitory input.

SAC-DSGC synaptic strength and asymmetric wiring is preserved in Sema6A$^{-/-}$ mice

One possible source of reduced SAC-mediated input to DSGCs in *Sema6A*$^{-/-}$ mice is a failure to form strong synaptic connections with DSGCs. Yet, paired recordings between SACs and DSGCs revealed that SAC-DSGC synaptogenesis and asymmetric connectivity were preserved in *Sema6A*$^{-/-}$ mice (Fig. 2A-E, compare with [11]). Furthermore, inhibitory conductance peaks and time courses between null side Control and *Sema6A*$^{-/-}$ pairs were not significantly different (Figure 2D,E). Note, we chose Sema6A$^{-/-}$ SACs close to the DSGC soma to ensure dendritic overlap. Therefore, we normalized the recorded conductances to the number of putative null-oriented synapses [9] and again found no significant difference in the relative strength per synaptic connection between Control and *Sema6A*$^{-/-}$ pairs (Figure 2F). These data indicate that subcellular SAC-DSGC synaptic specificity is unperturbed in *Sema6A*$^{-/-}$ mice, demonstrating that the developmental processes governing asymmetric SAC-DSGC wiring are independent of the morphology of the distal SAC dendritic arbor and Sema6A signaling.

Sema6A$^{-/-}$ SAC varicosities maintain direction selectivity

Asymmetric inhibition from SACs to DSGCs requires not only asymmetric wiring, but also a centrifugal motion preference of SAC GABA release sites at distal dendritic varicosities [13]. Therefore, we tested whether the decrease in null direction evoked inhibition measured in DSGCs of *Sema6A*$^{-/-}$ mice resulted from changes in the response properties of SAC varicosities to visual stimuli. First, voltage clamp recordings showed that light flashes evoked similar peak excitatory and inhibitory conductances in Control and Sema6A$^{-/-}$ SACs (Figure S2A,B). Second, two photon Ca^{2+} imaging revealed that Sema6A$^{-/-}$ SACs maintain the skewed distribution of excitatory inputs thought to underlie SAC varicosity direction selectivity (Figure S2C,D, [1, 5]). Third, varicosity Ca^{2+} responses to motion stimulation in Sema6A$^{-/-}$ SACs were equally as strong (Figure 3B), and, surprisingly, could be even more narrowly tuned (Figure 3A,C) than in Control SACs. Together, these data indicate that despite the shorter dendritic lengths (Figure S3D) of Sema6A$^{-/-}$ SAC dendrites, direction selective computational abilities were preserved.

Sema6A$^{-/-}$ SAC varicosities are not necessarily tuned to centrifugal motion

The antiparallel alignment of the preferred directions of SAC varicosities and their postsynaptic DSGCs is essential for generating tuned inhibitory input. Thus, although asymmetric SAC-DSGC wiring and direction selectivity in SAC dendrites are maintained in *Sema6A*$^{-/-}$ mice, we hypothesized that the increased dendritic tortuosity ([17], Figure 4A,E) in Sema6A$^{-/-}$ SACs may affect the interplay of these two circuit components. Therefore, we analyzed the DS tuning of varicosities in Sema6A$^{-/-}$ and Control SACs (Figure 4A) along the

preferred-null axis (defined by the orientation of the vector sum of the tuning curve) and along the soma-varicosity, or centrifugal, axis, which determines SAC wiring with DSGC subtypes. For Control SAC varicosities, direction selective tuning was equally strong along the soma-varicosity and preferred-null axes (Figure 4B,D), as expected by the radial symmetry of the dendrites. In contrast, for Sema6A$^{-/-}$ SACs, there was a significant difference in tuning between the two axes (Figure 4D). Varicosity directional tuning along the preferred-null axis was larger than that in Control SAC varicosities, while varicosity directional tuning along the soma-varicosity axis was significantly reduced compared to Control SAC varicosities (Figure 4B). This difference in Sema6A$^{-/-}$ SAC tuning was due to decreased Ca^{2+} transient amplitudes in response to centrifugal stimulation compared to responses during preferred direction stimulation (Figure 4C). Overall, the greater degree of dendritic tortuosity in Sema6A$^{-/-}$ SACs led to a significantly larger misalignment between the functional preferred-null axis and the anatomical soma-varicosity axis (Figure 4E). These results indicate that SACs in *Sema6A*$^{-/-}$ mice may no longer maximally release GABA in response to motion in their postsynaptic DSGCs' null direction.

Loss of inhibitory directional tuning in Sema6A$^{-/-}$ mice results primarily from reduced SAC dendritic density

Thus far, we have shown that SACs in *Sema6A*$^{-/-}$ mice synapse asymmetrically onto DSGCs and have directionally tuned dendrites, but that these processes are not always aligned. In addition, the reduced dendritic length of SACs in *Sema6A*$^{-/-}$ mice leads to a reduction of dendritic coverage (cell density x field area) from around 30 [17] to roughly 11 (Figure 5A). Does the loss of SAC dendritic coverage or the misalignment between functional and anatomical axes in Sema6A$^{-/-}$ SACs contribute more to the reduction in DSGC IPSC tuning? Using a simulation that accounted for the symmetric inhibitory contribution from non-SAC GABAergic amacrine cells [19, 20], we found that decreasing SAC dendritic coverage to Sema6A$^{-/-}$ SAC levels led to a large reduction in the asymmetric inhibitory inputs onto the DSGC that closely mimicked IPSC amplitudes recorded in *Sema6A*$^{-/-}$ mice (Figure 5B,C). Simulations in which SAC dendrites tiled the retina led to a complete abolishment of directional inhibitory input (Figure 5A-C). These results indicate that the loss in coverage factor alone would be sufficient to prevent direction selective signaling.

We then estimated how increasing the misalignment between the SAC-DSGC wiring axis and varicosity preferred directions contributes to a reduction in IPSC tuning at both WT and *Sema6A*$^{-/-}$ SAC coverage levels. When we assumed a random alignment between these two circuit components, IPSC directional tuning was completely abolished at all SAC coverage factors (Figures 5D-F). However, simulations using the experimentally observed differences in *Sema6A*$^{-/-}$ mice between the two axes (Figure 4), resulted in a smaller, but still significant, reduction in IPSC directional tuning (Figure 5D-F). Thus, we conclude that in *Sema6A*$^{-/-}$ mice the loss of DSGC directional tuning is explained primarily by the decreased SAC dendritic coverage [17], while synaptic input from varicosities on tortuous SAC dendritic arbors can further degrade the precise asymmetry of GABA release found in Control retinas.

SAC varicosity directional preferences determined near the end of the excitatory input distribution

We next sought to use the increased dendritic tortuosity of Sema6A$^{-/-}$ SAC dendrites to elucidate which portions of the SAC dendritic arbor were responsible for determining varicosity directional preference. Specifically, we compared varicosity preferred directions to the average dendritic orientation of different portions of the SAC dendrite, starting at the first branch from the soma (Figure 6A). The dendrites of Control SACs generally radiate straight out from the soma, and therefore Control SAC varicosity preferred directions aligned equally well with all average dendritic orientations calculated using segments distal to the first branch point (Figure 6A,B, gray). In contrast, for the more complex dendrites of Sema6A$^{-/-}$ SACs (Figure 4E, S3F), varicosity preferred directions aligned best to dendritic orientations calculated with segments distal to the fourth branch point (Figure 6A,B blue). These results were consistent across varicosity tuning strengths (Figure S3A). The fourth branch point is 90-120 μm away from the soma (roughly 70% of the SAC dendrite), corresponding to the most distal extent of bipolar cell inputs onto the SAC dendrite as determined by glutamate uncaging [1] and electron microscopy [2, 5] (Figure S3D,E). Indeed, when individual branch angles were considered, the orientation of the 4th order dendritic segment was most responsible for varicosity directional preference (Figure 6B, Figure S3B,C), indicating that the directional preference of SAC varicosities is determined by the local orientation of the last dendritic segment with glutamate receptors (Figure 6C). The implications of these results on current models of SAC directional computations are discussed below.

Discussion

These results show that DSGCs in *Sema6A*$^{-/-}$ mice have reduced ON directional tuning directly resulting from changes in SAC morphology, but not SAC-DSGC wiring or SAC dendritic computations. First, DSGCs lack directional tuning due to a weaker and more symmetric synaptic inhibitory input in *Sema6A*$^{-/-}$ mice. Second, paired recordings between Sema6A$^{-/-}$ SACs and DSGCs show that asymmetric wiring is preserved. Third, two-photon Ca^{2+} imaging of Sema6A$^{-/-}$ SAC varicosities shows that the intrinsic directional selectivity of SAC dendrites is preserved. Hence, we conclude that SAC morphology and spacing is critical for generating a highly overlapping plexus of dendrites required for DS computations. Finally, the increased dendritic tortuosity in Sema6A$^{-/-}$ SACs allowed us to determine that a relatively short portion of the distal half of the SAC dendritic arbor is sufficient for determining varicosity directional preference.

Implications for DS mechanisms

Our finding that the loss of DS in *Sema6A*$^{-/-}$ mice is due to an overall loss of SAC coverage is surprising given that SACs are among the most over-represented cell types in the retina, with coverage factors from 25-35 depending on the mouse strain [21]. While there is a dramatic loss of ON SAC dendritic coverage in *Sema6A*$^{-/-}$ mice, ON SACs and DSGCs still cofasciculate strongly [17]. Thus, one may expect that the remaining inhibition from SAC dendrites would be sufficient to generate direction selective responses, especially since asymmetric wiring and SAC varicosity tuning are still present (Figures 2,3). Indeed, SAC

mediated transmission alone is sufficient in WT mice to generate DS responses in DSGCs [22]. However, we found that this loss of coverage causes a significant reduction in IPSC asymmetry, likely disrupting the delicate balance between excitatory bipolar cell inputs and both inhibitory and excitatory SAC inputs onto DSGCs [22-24] leading to an increase in null direction evoked DSGC spiking.

In contrast, using a simple simulation, we found that the misalignment between the functional preferred-null axis and the anatomical soma-varicosity axis minimally impacted IPSC tuning in DSGCs of *Sema6A*$^{-/-}$ mice. However, when we repeated the simulation using a broader range of angles, we observed a dramatic loss of IPSC tuning (Figure 5). We postulate that this greater loss of IPSC tuning may in part explain the reduced IPSC tuning in Pcdhg$^{-/-}$mice, which have even more tortuous SAC dendrites but no reduction in coverage factor [14]. Hence, different manipulations of SAC morphology can impact DS computation via distinct mechanisms.

Implications for dendritic tuning

The subcellular directional computation in SAC dendrites emerges from the interplay of three potential mechanisms. The first mechanism is based on a proximally skewed distribution of excitatory bipolar cell inputs combined with the electronic properties of the thin SAC cable [1, 5] and assumes that SAC processes are electrically isolated from each other, a requirement recently proven critical for DS generation [12]. In this model, temporal summation of closely spaced glutamatergic inputs during motion towards the varicosities leads to a slightly larger membrane depolarization at distal dendrites than during motion towards the soma, in a manner first described by Rall [25]. This small difference is greatly amplified by the presence of nonlinear conductances located in the distal portion of the dendrite [12, 26, 27].

How much dendrite is necessary to perform this computation? By comparing SAC dendritic segment orientations to varicosity preferred directions, we found that the dendritic segment best aligned to varicosity preferred directions was distal to the fourth branch point (Figure 6), corresponding to the location of the most distal glutamatergic bipolar cell inputs onto the SAC (Figure S3E). These data suggest that sequential summation over only a small segment of glutamate receptors is sufficient to generate a depolarization that differentiates centrifugal from centripetal stimulation. Our results also suggest that the nonlinear conductance underlying the conversion of a weak directional voltage difference to a strong dendritic directional preference is located distal to the glutamate receptors but proximal to most of the release sites. This configuration ensures a consistent level of direction selectivity over all varicosities due to the dendritic end effect [1].

The second mechanism for SAC dendritic DS is based on lateral inhibition between SACs [28, 53]. This mutual inhibition enhances the directionality of SAC dendrites [1, 15], but is not the primary component of the computation [13], playing a more critical role under conditions of high contrast [5] or noisy backgrounds [29]. Since SAC-SAC connections are formed in proximal dendritic segments [5], only the distal third of SAC dendrites in Sema6A$^{-/-}$ SACs fail to exhibit self-avoidance, inhibitory conductances in Sema6A$^{-/-}$ SACs are the same as in Controls, and Sema6A$^{-/-}$ SAC varicosities are well tuned (Figure 3),

inhibitory SAC-SAC connections are not likely to be a major factor in affecting DS in Sema6A$^{-/-}$ mice.

The third mechanism is based on the arrangement of pre-synaptic bipolar cells with different kinetics. Disruption of bipolar cell wiring onto SACs certainly reduces direction selectivity in DSGCs [30, 31], but the presence of distance dependent differences in excitatory input kinetics required for “space-time wiring” in ON SACs has remained controversial [2, 5, 32, 33]. Two of our findings in Sema6A$^{-/-}$ mice suggest this model is not a major contributor in the ON pathway. First, bipolar kinetics vary with IPL lamination [34, 35] and Sema6A$^{-/-}$ SACs no longer stratify in a single layer ([17], Figure S2A,B), but strong SAC dendritic DS is maintained (Figure 3). Second, the “space-time” model requires both proximal and distal excitatory inputs to generate DS, but we find that SAC tuning is most well aligned with the orientation of distal dendritic branches (Figure 6) that are not likely to receive spatially offset inputs from two different BP cell subtypes.

In conclusion, our results reveal a central role for the high SAC coverage factor in generating direction selectivity. Understanding the genetic basis [36] and cellular mechanisms [37, 38] underlying the creation of the dense SAC plexus may help shed light on why some cell classes are overrepresented in the retina and other brain regions. Moreover, the altered morphology of Sema6A$^{-/-}$ SACs has revealed a dissociation within the SAC arbor between connectivity and intrinsic directional preference. While asymmetric wiring with DSGCs is likely instructed by the segregation of different signaling molecules at proximal SAC dendrites [39, 40], we find that the directional preferences of varicosities on that dendrite are determined at a more distal location. Further functional analysis of morphological alterations in SACs [15, 54] and other neurons [14, 41] can help elucidate the underlying cellular and molecular mechanisms that link dendritic structure, wiring, and computation.

Contact For Reagent and Resource Sharing

Further information and requests for reagents may be directed and will be fulfilled by the Lead Contact and corresponding author Marla B. Feller (mfeller@berkeley.edu).

Experimental Model and Subject Details

Animals

Mice used in this study were aged from p25-120 and were of both sexes. To target DSGCs and SACs, ChAT-Cre/nGFP/TrHr (CNT) mice were generated by crossing together three mouse lines: (1) B6.129S6-ChATtm1(cre)lowl/J (Jackson Laboratories), with Cre driven by the endogenous choline acetyltransferase promoter, (2) B6.129-Gt(ROSA)26Sor^{tm1Joe}/J (Jackson Laboratories), with a nuclear-localized GFP-lacZ function protein downstream of a loxP-flanked STOP sequence, and (3) TrHr-GFP mice [42], which express GFP in nasal preferring DSGCs [43]. CNT mice then were crossed to a Sema6A gene trap mouse [18, 44] in which a PLAP secretory trap vector was inserted at the codon for amino acid 473 in the semaphorin domain. For all experiments, Control animals were CNTSema6A$^{+/+}$ or CNTSema6A$^{+/-}$ littermates of CNTSema6A$^{-/-}$ animals. All experiments involved recording

from 1-5 cells or cell pairs from at least 3 animals of either sex for each genotype. All animal procedures were approved by the UC Berkeley Institutional Animal Care and Use Committee and conformed to the NIH *Guide for the Care and Use of Laboratory Animals*, the Public Health Service Policy, and the SFN Policy on the Use of Animals in Neuroscience Research.

Method Details

Retina Preparation

Mice were anesthetized with isoflurane and decapitated. Retinas were dissected from enucleated eyes in oxygenated (95% O2/ 5% CO2) Ames' media (Sigma) for light responses or ACSF (in mM, 119 NaCl, 2.5 KCl, 1.3 $MgCl_2$, 1 K_2HPO_4, 26.2 $NaHCO_3$, 11 D-glucose, and 2.5 $CaCl_2$) for paired recordings. Retinal orientation was determined as described previously [45]. Isolated retinas were cut into dorsal and ventral halves, mounted over a 1–2 mm^2 hole in nitrocellulose filter paper (Millipore) with the photoreceptor layer side down, and stored in oxygenated Ames' media or ACSF until use (maximum 10 h). Filter paper mounted retinas in which dorsal-ventral orientation was tracked will be referred to as oriented retinas.

2P targeted recordings and visual stimulation

Oriented retinas were placed under the microscope in oxygenated Ames' medium at 32–34°C. Identification and recordings from GFP^+ cells were performed as described previously [45]. In brief, GFP^+ cells were identified using a custom-modified two-photon microscope (Fluoview 300; Olympus America) tuned to 920 nm to minimize bleaching of photoreceptors. The inner limiting membrane above the targeted cell was dissected using a glass electrode. Cell attached voltage clamp recordings were performed with a new glass electrode (4-5 MΩ) filled with internal solution containing the following (in mM): 110 $CsMeSO_4$, 2.8 NaCl, 20 HEPES, 4 EGTA, 5 TEA-Cl, 4 Mg-ATP, 0.3 Na_3GTP, 10 Na_2Phosphocreatine, 5 QX-Cl (pH = 7.2 with CsOH, osmolarity = 290, ECl^- = -60 mV). After cell attached recordings of spikes, whole cell recordings were performed with the same pipette after obtaining a GΩ seal. Holding voltages for measuring excitation and inhibition after correction for the liquid junction potential (-10 mV) were 0 mV and -60 mV, respectively. Signals were acquired using pCLAMP 9 recording software and a Multiclamp 700A amplifier (Molecular Devices), sampled at 20 kHz, and low-pass filtered at 6 kHz.

For visual stimulation of DSGCs, broad-band visible light ranging from 470 to 620 nm was generated using an OLED display (SVGA Rev2 OLED-XL; eMagin) displaying custom stimuli created using MATLAB software with the Psychophysics Toolbox. These images were projected onto the photoreceptor layer through the same 60× objective used to target cells (Olympus LUMPlanFl/IR 360/0.90W), which was focused onto the photoreceptor layer once the cell attached recording configuration was achieved. The illumination radius on the retina was ~300 μm, which was significantly smaller than in previous recordings from DSGCs in $Sema6A^{-/-}$ mice [17] to limit the modulation of DSGC responses by inhibitory wide-field amacrine cells [46]. Moving bars (320 × 650 μm) were presented to the cell with

both positive and negative contrasts at 500 μm/sec in three trials of eight pseudorandomized directions parallel to the longer axis of the bar.

Paired voltage clamp recordings and imaging

Oriented retinas were placed under the microscope in oxygenated ACSF containing the following excitatory neurotransmitter blockers (in mM): 0.05 AP5, 0.02 DNQX and 0.008 DHβE. GFP^+ DSGCs and $nGFP^+$ SACs were identified under 2 photon illumination and targeted as above. Whole cell voltage clamp recordings were achieved for a given DSGC before targeting SACs. Note, we targeted SACs in $Sema6A^{-/-}$ mice with small inter-soma distances with the patched DSGC to ensure some degree of dendritic overlap and thus synaptic connectivity. Recordings from DSGCs were performed with glass electrodes (3-5 MΩ) filled with internal solution containing the following (in mM): 110 $CsMeSO_4$, 2.8 NaCl, 20 HEPES, 4 EGTA, 5 TEA-Cl, 4 Mg-ATP, 0.3 Na_3GTP, 10 $Na_2Phosphocreatine$, 0.025 AlexaFluor488 (pH = 7.2 with CsOH, osmolarity = 290, ECl^- = -74 mV). Recordings from SACs were performed similarly, except the internal solution EGTA concentration was 0.1 mM [10] and AlexaFluor594 was used. To calculate SAC-DSGC synaptic conductances, DSGC were held at voltage potentials ranging from -100 mV to +20 mV while SACs were depolarized three times from the holding potential (-70 mV) to 0 mV for 50 ms. After recording synaptic currents, 2 photon 1024×1024 image stacks of the dye filled cells were acquired with 780 nm excitation, using a 0.5 μm step size.

Imaged cells were manually reconstructed using the FIJI plugin Simple Neurite Tracer. After cells were traced, the ‘fill out’ function was used until a volume rendering of the entire cell was created. The resulting volumes for the two cells were exported as .tif image stacks and then imported into Imaris 9 (Bitplane), where the colocalization between the two volumes was calculated and the results were used to create a new colocalization channel. The ‘Spots’ function of Imaris was used on this colocalization channel to identify sites of overlap. To identify putative synaptic sites, we manually selected Spots on the outer third of SAC dendrites located within 67° on either side of the null direction (vertex at the SAC soma) [9]. The number of these putative synapses were then compared to the calculated conductances using regression analysis.

SAC Light Responses

Filter paper mounted retinas were placed under a custom 2-photon microscope [1] in oxygenated Ames' medium at 32–34°C. $nGFP^+$ SACs were identified under 2 photon illumination (930 nm) or by their small round somas, characteristic responses to voltage steps, and/or post-hoc imaging.

For voltage clamp experiments, glass electrodes (3-5 MΩ) filled with internal solution containing the following (in mM): 110 $CsMeSO_4$, 2.8 NaCl, 20 HEPES, 4 EGTA, 5 TEA-Cl, 4 Mg-ATP, 0.3 Na_3GTP, 10 $Na_2Phosphocreatine$, 0.025 AlexaFluor594 (pH = 7.2 with CsOH, osmolarity = 290, ECl^- = -73 mV) were used to target SACs identified under a 40× ACHROPLAN water immersion objective (0.80 NA, Zeiss). Light responses recordings were performed with at least 5 different holding potentials ranging from -100 to +20 mV after correction for the liquid junction potential (-12mV). Visual stimuli were created on a

670 × 550 μm patch of retina by projecting an LED light source (M470L2, Thorlabs, Inc.) through a DMD (Cell5500-Fiber, Digital Light Innovations) controlled by custom software (Psychophysics Toolbox) that were focused through the condenser lens onto the photoreceptors. Prior to each experiment, visual stimuli were aligned to the middle of the 2-photon imaging field and the photoreceptors by inserting a pipette filled with Alexa594 and positioning it at the focal plane of the photoreceptors (measured by IR imaging) and the middle of the 2-photon imaging window. A small spot (5 μm radius) was projected and aligned to the tip of the pipette via focusing or shifting the condenser in the XY plane. SACs were presented with three repetitions of a 400 μm diameter spots centered on the SAC soma at each holding potential. After recording, full field (196 × 196 μm) images of SAC morphology (512 × 512, 8ms/line, bidirectional scanning) were obtained by tuning the laser to 850 nm to analyze SAC dendritic arbor length.

For Ca^{2+} imaging experiments, SACs were filled with Oregon Green 488 BAPTA-1 (OGB1, Life Technologies) via a sharp electrode as per [5]. Briefly, borosilicate glass (I.D.=1.1, O.D.=1.5 mm) electrodes were first pulled to a resistance of 100-150 MΩ and then were bent (such that electrode tips were perpendicular to the retinal surface when inserted into the headstage) by placing the electrode tangentially to a water bubble and heating it with a microforge. Bent electrodes were filled with 15 mM OGB1 and placed above the targeted SAC under infrared illumination. 2 photon illumination was used to guide the electrode tip through the inner limiting membrane into the targeted SAC and visualize cell filling. Ionotophoresis of OGB1 was achieved with negative current pulses (-10 to -20 nA, 500 ms) and electrodes were withdrawn as cell bodies began to fill. Filled SACs were left to recover for 30-60 minutes before imaging. Multiple, non-overlapping SACs were often filled within the same filter paper hole.

Simultaneous Ca^{2+} imaging and visual stimulation were performed generally as in [1] under a 60× LUMPlanFL N water immersion objective (1.00 NA, Olympus).

For spot response receptive field mapping experiments, visual stimuli were aligned to the center of the 2-photon imaging field. Spot positions were defined by taking a low intensity z-stack (930 nm) of the filled SAC, picking a varicosity at the end of a dendrite for imaging, and then identifying five points along that dendrite roughly corresponding to 0, 25, 50, 75, and 100% of total dendritic length. Visual stimuli were presented after 20 s of imaging to allow photoreceptors to adapt to the scanning laser [47]. Three trials of 12.5 μm radius spots centered at each of these points were presented in pseudorandom order for 1 sec each with 6 s in between. SAC varicosities were imaged using a 930nm excitation wavelength and images were acquired at 11.84 Hz (64 × 64 pixels, 1ms/line, bidirectional scanning).

For direction selectivity experiments visual stimuli were aligned to the top left corner of the 2-photon imaging field. After filled SACs recovered, cells were positioned with their soma at the center of the stimulus field and 26 × 26 μm ROIs were selected at various positions along the SAC arbor. SAC dendrites were imaged using a 930 nm excitation wavelength and images were acquired at 7.58 Hz (256 × 100 pixels, 1ms/line, bidirectional scanning). Visual stimuli consisted of 3 trials of moving bars (400 × 200 μm) moving at 500 μm/sec in eight pseudorandomized directions parallel to the shorter axis of the bar across the entire stimulus

plane. SACs that did not exhibit Ca^{2+} responses to initial laser scanning were excluded from further experimentation.

For all Ca^{2+} imaging experiments, after functional imaging, full field (131 × 131 μm), high resolution images of SAC morphology (512 × 512, 4ms/line, bidirectional scanning) were obtained by tuning the laser to 800 nm to increase OGB1 excitation. The objective was moved and multiple images were acquired and stitched together using 3D stitching (FIJI), if required, to trace imaged varicosities back to the soma. Dendritic morphology was manually reconstructed using Simple Neurite Tracer (FIJI). Imaged varicosities and the cell soma were labeled on the Simple Neurite tracing of each SAC with SWC identifiers. Cell reconstructions were exported as .SWC files and imported into the TREES toolbox [48, 49] in Matlab for further analysis.

IPSC simulation

To simulate directional SAC-DSGC inhibitory synaptic transmission we first assigned pre-synaptic SAC release sites to a location on the null half of the SAC arbor (-90° to 90° with 0° representing the DSGC's null direction). The number of SAC release sites varied from 1-100, with 1 representing tiled SAC input and 100 representing the endogenous SAC coverage factor of 30 (Figure 5A). The direction of maximal GABA release for each simulated varicosity was then offset from its anatomical angle by randomly drawing, with replacement, from the experimentally observed differences between preferred-null (PN) and soma-varicosity (SV) axes orientations for Control or Sema6A$^{-/-}$ SAC (Figure 4). Varicosity synaptic release directions (anatomical angle + PN-SV axes offset) were binned into 45 degree increments to simulate the highest resolution possible in our experiments using 8 directions of stimulus motion. Synaptic release from each varicosity caused a 18 pA current in the simulated DSGC, based on quantal recordings [10] and our normalization of inhibitory conductances to putative release sites (Figure 2F). Synaptic currents magnitudes were then summed across bins and added to a radially symmetric 400 pA current from non-SAC GABAergic amacrine cells [19, 20] to create a synaptic release tuning curve. This simulation was repeated 1000 times to generate the average tuning curves and the distributions of normalized tuning curve vector sums in Figure 5. For the Random simulation, PN-SV axes offsets were randomly drawn, with replacement, from the distribution of all angles ranging from -359° to 359°.

Quantification and Statistical Analysis

DSGC Light Responses

For cell attached DSGC recordings, spike counts were calculated by bandpass filtering traces (0.08-2 kHz) and manually identifying a threshold value for spikes on the filtered traces. Local minima below threshold that did not violate refractory period criteria (0.001 s) were counted as spikes. ON and OFF responses were defined as spikes occurring within a 900 ms time window starting right before the presentation of the leading or trailing edge of the stimulus. The average spike counts across the 3 trials were used to calculate the vector sum of the spike responses. Preferred directions for both ON and OFF responses used to calculate

average spike counts in Fig S1 were defined as the angle of the vector sum of spike responses for the OFF response.

For voltage clamp DSGC recordings, traces were first average across the 3 trials for each direction and inspected to ensure consistency of responses. Average traces were baseline subtracted based on the last 500 ms of recording or a user defined interval after manual inspection. Peak currents were calculated from average baseline subtracted traces and were the maximal (IPSC) or minimal (EPSC) points during the 900 ms window described above. Charge transfers were calculated as the integral of the average baselined traces during the 900 ms window. The peak currents were used to calculate the vector sum of the current responses. Preferred directions for both ON and OFF responses used to calculate peak responses reported in Supplementary Figure 1 were defined as 180° + the angle of the vector sum of OFF peak IPSCs, or the angle of the vector sum of OFF peak EPSCs if IPSCs were not recorded in that cell.

Paired Recordings

Inhibitory conductance analysis of paired SAC-DSGC recordings was performed in IGOR Pro using the algorithm described in [50]. Briefly, sweeps at each DSGC holding potential were averaged and then the baseline holding current (defined as the average current prior to SAC stimulation) was subtracted from each average trace. We compensated for the series resistance (R_s) by measuring the series and input resistance (R_{in}) from a -5 mV pulse at the end of each trace. We used the following equations for compensation of the recorded current (I_m) and the holding potential (V_h):

$$I_{syn}(t) = (R_{in} + R_s)/R_{in} * I_m(t) \quad (1)$$

$$V(t) = V_h - I_m(t) * R_s \quad (2)$$

Then we fit a line to the IV data (I_{syn} vs.V) for the various holding potentials at each time point (t) in the trace. The slopes and intercepts of these lines were used to calculate the inhibitory conductance gT (the slope) and the reversal potential Vrev (-intercept/slope). We controlled for quality of recording by requiring an R^2 value for the linear fit of the IV data above 0.85.

SAC Light Response Recordings

Conductance analysis of SAC light responses was performed similarly using a custom written script in Matlab based off of [51]. Briefly, sweeps at each SAC holding potential were averaged and then the baseline holding current (200ms before light stimulation) was subtracted from each average trace. We compensated for the series resistance (R_s) and input resistance (R_{in}) from a -5 mV pulse at the end of each trace as above. The total conductance gT and reversal potential Vrev were calculated based on the IV data as above and recording quality was controlled by requiring an R^2 value for the linear fit of the IV data above 0.9.

Inhbitiory (gI) and excitatory conductances (gE) were separated based on the reversal potentials for inhibition (Vi = -73 mV) and excitation (Ve = 0 mV) and the following equations:

$$gI(t) = [gT(t) * (Vrev(t) - Ve)]/(Vi - Ve) \quad (3)$$

$$gE(t) = [gT(t) * (Vrev(t) - Vi)]/(Ve - Vi) \quad (4)$$

SAC Ca^{2+} Light Responses and morphology

For spot response receptive field mapping experiments, SAC varicosity ROIs were identified using a custom macro (FIJI). A summed intensity projection was created from movie of the imaged varicosity, a Gaussian blur was applied to remove sharp edges (sigma = 1.5), and the ROI center was selected using the default thresholding algorithm. This ROI mask was dilated twice to ensure even sampling throughout the movie. Background ROIs were selected on the same Gaussian blurred image, but using the triangle threshold algorithm. SAC varicosity Ca^{2+} responses were analyzed with custom Matlab scripts. Average fluorescence intensity (F) was calculated for each ROI and background subtracted using the average intensity of the background ROI defined above for each frame. Background subtracted F traces were segmented by stimulus presentations. ΔF/F traces for each stimulus were calculated using the fluorescence intensity during the last half of the inter-trial period before the stimulus (3 s) and averaged together based on stimulus location. Stimulus center positions were matched to the closest point on the imported SAC dendrite reconstruction using custom Matlab scripts. Moving averages and standard deviations were calculated using the Average Waves function in Igor Pro.

For direction selectivity experiments, SAC varicosity ROIs were identified using a custom macro (FIJI). Images were 3D median filtered to denoise, baseline subtracted via a 100-frame z median filter, and then bandpass filtered (2-15 pixels). The processed image was thresholded via the Triangle algorithm, with upper and lower bounds manually defined, and the background was subtracted. Potential individual varicosities were identified as local maxima on the average projection of the background-subtracted stack via a user defined threshold level and a subsequent watershed step filled them out. The resulting varicosity and background ROI masks were imported into Matlab for further processing.

SAC varicosity Ca^{2+} responses were analyzed with custom Matlab scripts. Average fluorescence intensity (F) was calculated for each ROI and background subtracted using the average intensity of the background ROI defined above for each frame. Background subtracted F traces for each ROI were segmented by stimulus presentations and the F traces for each stimulus direction were averaged together. ΔF/F traces were calculated using the fluorescence intensity during the first 2/5 of the time in between stimulus presentations as the baseline. Ca^{2+} responses to a given stimulus were defined as the maximal ΔF/F during stimulus presentation. ROIs were excluded from further analysis if their baseline

background-subtracted fluorescence was <1 or the maximal responses to ≥4 stimulus presentations was not >2.5 standard deviations of the total ΔF/F trace for that stimulus direction. Vector sums were calculated from these maximal ΔF/F values for each ROI, with the preferred direction defined as the angle of the vector sum. Direction selective indices were calculated using the formula:

$$DSI = \frac{(preferred - null)}{preferred} \quad (3)$$

where preferred is the peak Ca^{2+} transient in response to the stimulus moving in the direction closest to the preferred direction and null is the Ca^{2+} transient in response to the stimulus moving oppositely. For outward vs. inward calculation, preferred direction corresponded to the stimulus moving in the direction closest to that of the Euclidean angle described below.

Imaged ROIs were matched to their respective locations on the imported SAC reconstruction using custom Matlab scripts utilizing the TREES toolbox [48, 49]. For each imaged varicosity, the Euclidean angle from the SAC soma to that varicosity was calculated using the point of transition from soma to dendrites in the tree. Average dendritic angles were calculated by first calculating the angle and distance from a dendritic branch point to the next branch point along that path, and then taking a vector sum of these angles and distances. Tortuosity was computed as the path length from the soma to a varicosity divided by the length of the Euclidean distance from soma to varicosity.

To determine how much of the variance in the varicosity directional preference is explained by different SAC dendritic branches we used a series of restricted linear regression models in which one dendritic branch was allowed to vary while holding the other branch angles at their median. Linear regressions were performed individually on the sine and cosine of dendritic branch and varicosity directional preference data and the inverse tangent of the resulting predictors were used to compute circular correlations [52] between the predicted and measured varicosity directional preferences. Regression models were validated with 10-fold cross validation by using a random sample of 90% of the data to fit the linear regression models and the remaining 10% of the data to calculate circular correlations. The model was bootstrapped 5000 times to get confidence intervals of the cross-validated circular correlations.

Statistics

Statistical tests used are indicated in the figure legends. All tests were two-sided. We report exact p values for all tests in which $p > 0.001$.

Data and Software Availability

The datasets generated during and/or analyzed during the current study and all custom scripts and functions generated or used during the current study are available from the corresponding author on request.

Supplementary Material

Refer to Web version on PubMed Central for supplementary material.

Acknowledgments

We thank Alex Kolodkin for the generous gift of the Sema6A$^{-/-}$ mice, Keven Laboy-Juárez for help with circular regression analysis, Benjamin E. Smith for help with Ca^{2+} imaging data analysis, Stephen G. Brohawn for lending his microforge, the Berkeley Molecular Imaging Center for image analysis software, and members of the Feller Lab for commenting on the manuscript. R.D.M. was supported by National Science Foundation (NSF) Grant DGE 1106400 and the UC Dissertation Fellowship and M.B.F. and R.D.M. were supported by NIH ROI1EY019498, RO1EY013528, and P30EY003176.

References

1. Vlasits AL, Morrie RD, Tran-Van-Minh A, Bleckert A, Gainer CF, DiGregorio DA, Feller MB. A Role for Synaptic Input Distribution in a Dendritic Computation of Motion Direction in the Retina. Neuron. 2016; 89:1317–1330. [PubMed: 26985724]
2. Greene MJ, Kim JS, Seung HS, EyeWirers. Analogous Convergence of Sustained and Transient Inputs in Parallel On and Off Pathways for Retinal Motion Computation. CellReports. 2016; 14:1892–1900.
3. Kim JS, Greene MJ, Zlateski A, Lee K, Richardson M, Turaga SC, Purcaro M, Balkam M, Robinson A, Behabadi BF, et al. Space-time wiring specificity supports direction selectivity in the retina. Nature. 2014; 509:331–336. [PubMed: 24805243]
4. Famiglietti EV. Synaptic organization of starburst amacrine cells in rabbit retina: analysis of serial thin sections by electron microscopy and graphic reconstruction. J Comp Neurol. 1991; 309:40–70. [PubMed: 1894768]
5. Ding H, Smith RG, Poleg-Polsky A, Diamond JS, Briggman KL. Species-specific wiring for direction selectivity in the mammalian retina. Nature. 2016; 535:105–110. [PubMed: 27350241]
6. Reese BE, Keeley PW. Design principles and developmental mechanisms underlying retinal mosaics. Biological Reviews. 2015; 90:854–876. [PubMed: 25109780]
7. Mauss AS, vlasits A, Borst A, Feller M. Visual Circuits for Direction Selectivity. Annu Rev Neurosci. 2017; 40:211–230. [PubMed: 28418757]
8. Vaney DI, Sivyer B, Taylor WR. Direction selectivity in the retina: symmetry and asymmetry in structure and function. Nat Rev Neurosci. 2012; 13:194–208. [PubMed: 22314444]
9. Briggman KL, Helmstaedter M, Denk W. Wiring specificity in the direction-selectivity circuit of the retina. Nature. 2011; 471:183–188. [PubMed: 21390125]
10. Morrie RD, Feller MB. An Asymmetric Increase in Inhibitory Synapse Number Underlies the Development of a Direction Selective Circuit in the Retina. J Neurosci. 2015; 35:9281–9286. [PubMed: 26109653]
11. Wei W, Hamby AM, Zhou K, Feller MB. Development of asymmetric inhibition underlying direction selectivity in the retina. Nature. 2011; 469:402–406. [PubMed: 21131947]
12. Koren D, Grove JCR, Wei W. Cross-compartmental Modulation of Dendritic Signals for Retinal Direction Selectivity. Neuron. 2017; 95:914–927.e4. [PubMed: 28781167]
13. Euler T, Detwiler PB, Denk W. Directionally selective calcium signals in dendrites of starburst amacrine cells. Nature. 2002; 418:845–852. [PubMed: 12192402]
14. Lefebvre JL, Kostadinov D, Chen WV, Maniatis T, Sanes JR. Protocadherins mediate dendritic self-avoidance in the mammalian nervous system. Nature. 2012; 488:517–521. [PubMed: 22842903]
15. Kostadinov D, Sanes JR. Protocadherin-dependent dendritic self-avoidance regulates neural connectivity and circuit function. Elife. 2015; 4
16. Koropouli E, Kolodkin AL. Semaphorins and the dynamic regulation of synapse assembly, refinement, and function. Current Opinion in Neurobiology. 2014; 27C:1–7.

17. Sun LO, Jiang Z, Rivlin-Etzion M, Hand R, Brady CM, Matsuoka RL, Yau KW, Feller MB, Kolodkin AL. On and Off Retinal Circuit Assembly by Divergent Molecular Mechanisms. Science. 2013; 342:1241974–1241974. [PubMed: 24179230]
18. Leighton PA, Mitchell KJ, Goodrich LV, Lu X, Pinson K, Scherz P, Skarnes WC, Tessier-Lavigne M. Defining brain wiring patterns and mechanisms through gene trapping in mice. Nature. 2001; 410:174–179. [PubMed: 11242070]
19. Park SJH, Borghuis BG, Rahmani P, Zeng Q, Kim IJ, Demb JB. Function and Circuitry of VIP+ Interneurons in the Mouse Retina. J Neurosci. 2015; 35:10685–10700. [PubMed: 26224854]
20. Pei Z, Chen Q, Koren D, Giammarinaro B, Ledesma HA, Wei W. Conditional Knock-Out of Vesicular GABA Transporter Gene from Starburst Amacrine Cells Reveals the Contributions of Multiple Synaptic Mechanisms Underlying Direction Selectivity in the Retina. J Neurosci. 2015; 35:13219–13232. [PubMed: 26400950]
21. Keeley PW, Whitney IE, Raven MA, Reese BE. Dendritic spread and functional coverage of starburst amacrine cells. J Comp Neurol. 2007; 505:539–546. [PubMed: 17924572]
22. Sethuramanujam S, McLaughlin AJ, deRosenroll G, Hoggarth A, Schwab DJ, Awatramani GB. A Central Role for Mixed Acetylcholine/GABA Transmission in Direction Coding in the Retina. Neuron. 2016; 90:1243–1256. [PubMed: 27238865]
23. Sethuramanujam S, Yao X, deRosenroll G, Briggman KL, Field GD, Awatramani GB. “Silent” NMDA Synapses Enhance Motion Sensitivity in a Mature Retinal Circuit. Neuron. 2017; 96:1099–1111.e3. [PubMed: 29107522]
24. Poleg-Polsky A, Diamond JS. Retinal Circuitry Balances Contrast Tuning of Excitation and Inhibition to Enable Reliable Computation of Direction Selectivity. J Neurosci. 2016; 36:5861–5876. [PubMed: 27225774]
25. Rall W. Distinguishing theoretical synaptic potentials computed for different soma-dendritic distributions of synaptic input. J Neurophysiol. 1967; 30:1138–1168. [PubMed: 6055351]
26. Lee S, Kim K, Zhou ZJ. Role of ACh-GABA cotransmission in detecting image motion and motion direction. Neuron. 2010; 68:1159–1172. [PubMed: 21172616]
27. Oesch NW, Taylor WR. Tetrodotoxin-resistant sodium channels contribute to directional responses in starburst amacrine cells. PLoS ONE. 2010; 5:e12447. [PubMed: 20805982]
28. Lee S, Zhou ZJ. The synaptic mechanism of direction selectivity in distal processes of starburst amacrine cells. Neuron. 2006; 51:787–799. [PubMed: 16982423]
29. Chen Q, Pei Z, Koren D, Wei W. Stimulus-dependent recruitment of lateral inhibition underlies retinal direction selectivity. Elife. 2016; 5:4481.
30. Shi Z, Trenholm S, Zhu M, Buddingh S, Star EN, Awatramani GB, Chow RL. Vsx1 Regulates Terminal Differentiation of Type 7 ON Bipolar Cells. J Neurosci. 2011; 31:13118–13127. [PubMed: 21917795]
31. Duan X, Krishnaswamy A, la Huerta De I, Sanes JR. Type II Cadherins Guide Assembly of a Direction-Selective Retinal Circuit. Cell. 2014; 158:793–807. [PubMed: 25126785]
32. Fransen JW, Borghuis BG. Temporally Diverse Excitation Generates Direction-Selective Responses in ON- and OFF-Type Retinal Starburst Amacrine Cells. Cell Reports. 2017; 18:1356–1365. [PubMed: 28178515]
33. Stincic T, Smith RG, Taylor WR. Time course of EPSCs in ON-type starburst amacrine cells is independent of dendritic location. The Journal of Physiology. 2016; 594:5685–5694. [PubMed: 27219620]
34. Borghuis BG, Marvin JS, Looger LL, Demb JB. Two-photon imaging of nonlinear glutamate release dynamics at bipolar cell synapses in the mouse retina. J Neurosci. 2013; 33:10972–10985. [PubMed: 23825403]
35. Baden T, Berens P, Bethge M, Euler T. Spikes in Mammalian Bipolar Cells Support Temporal Layering of the Inner Retina. Current Biology. 2013; 23:48–52. [PubMed: 23246403]
36. Whitney IE, Keeley PW, St John AJ, Kautzman AG, Kay JN, Reese BE. Sox2 regulates cholinergic amacrine cell positioning and dendritic stratification in the retina. J Neurosci. 2014; 34:10109–10121. [PubMed: 25057212]

37. Farajian R, Raven MA, Cusato K, Reese BE. Cellular positioning and dendritic field size of cholinergic amacrine cells are impervious to early ablation of neighboring cells in the mouse retina. Vis Neurosci. 2004; 21:13–22. [PubMed: 15137578]
38. Kay JN, Chu MW, Sanes JR. MEGF10 and MEGF11 mediate homotypic interactions required for mosaic spacing of retinal neurons. Nature. 2012; 483:465–469. [PubMed: 22407321]
39. Morrie RD, Feller MB. Development of synaptic connectivity in the retinal direction selective circuit. Current Opinion in Neurobiology. 2016; 40:45–52. [PubMed: 27380013]
40. Yonehara K, Fiscella M, Drinnenberg A, Esposti F, Trenholm S, Krol J, Franke F, Scherf BG, Kusnyerik A, Müller J, et al. Congenital Nystagmus Gene FRMD7 Is Necessary for Establishing a Neuronal Circuit Asymmetry for Direction Selectivity. Neuron. 2016; 89:177–193. [PubMed: 26711119]
41. Joo W, Hippenmeyer S, Luo L. Dendrite morphogenesis depends on relative levels of NT-3/TrkC signaling. Science. 2014; 346:626–629. [PubMed: 25359972]
42. Gong S, Zheng C, Doughty ML, Losos K, Didkovsky N, Schambra UB, Nowak NJ, Joyner A, Leblanc G, Hatten ME, et al. A gene expression atlas of the central nervous system based on bacterial artificial chromosomes. Nature. 2003; 425:917–925. [PubMed: 14586460]
43. Rivlin-Etzion M, Zhou K, Wei W, Elstrott J, Nguyen PL, Barres BA, Huberman AD, Feller MB. Transgenic mice reveal unexpected diversity of on-off direction-selective retinal ganglion cell subtypes and brain structures involved in motion processing. J Neurosci. 2011; 31:8760–8769. [PubMed: 21677160]
44. Mitchell KJ, Pinson KI, Kelly OG, Brennan J, Zupicich J, Scherz P, Leighton PA, Goodrich LV, Lu X, Avery BJ, et al. Functional analysis of secreted and transmembrane proteins critical to mouse development. Nat Genet. 2001; 28:241–249. [PubMed: 11431694]
45. Wei W, Elstrott J, Feller MB. Two-photon targeted recording of GFP-expressing neurons for light responses and live-cell imaging in the mouse retina. Nat Protoc. 2010; 5:1347–1352. [PubMed: 20595962]
46. Hoggarth A, McLaughlin AJ, Ronellenfitch K, Trenholm S, Vasandani R, Sethuramanujam S, Schwab D, Briggman KL, Awatramani GB. Specific Wiring of Distinct Amacrine Cells in the Directionally Selective Retinal Circuit Permits Independent Coding of Direction and Size. Neuron. 2015; 86:276–291. [PubMed: 25801705]
47. Denk W, Detwiler PB. Optical recording of light-evoked calcium signals in the functionally intact retina. Proc Natl Acad Sci USA. 1999; 96:7035–7040. [PubMed: 10359834]
48. Cuntz H, Forstner F, Borst A, Häusser M. One Rule to Grow Them All: A General Theory of Neuronal Branching and Its Practical Application. PLoS Comput Biol. 2010; 6:e1000877. [PubMed: 20700495]
49. Cuntz H, Forstner F, Borst A, Häusser M. The TREES toolbox--probing the basis of axonal and dendritic branching. Neuroinform. 2011; 9:91–96.
50. Taylor WR, Vaney DI. Diverse synaptic mechanisms generate direction selectivity in the rabbit retina. J Neurosci. 2002; 22:7712–7720. [PubMed: 12196594]
51. Wehr M, Zador AM. Balanced inhibition underlies tuning and sharpens spike timing in auditory cortex. Nature. 2003; 426:442–446. [PubMed: 14647382]
52. Berens P. CircStat: a MATLAB toolbox for circular statistics. Journal of Statistical Software. 2009; 31:1–21.
53. Poleg-Polsky A, Ding H, Diamond JS. Functional Compartmentalization within Starburst Amacrine Cell Dendrites in the Retina. Cell Rep. 2018; 22(11):2898–2908. [PubMed: 29539419]
54. Ing-Esteves S, Kostadinov D, Marocha J, Sing AD, Joseph KS, Laboulaye MA, Sanes JR, Lefebvre JL. Combinatorial Effects of Alpha- and Gamma-Protocadherins on Neuronal Survival and Dendritic Self-Avoidance. J Neurosci. 2018; 14;38(11):2713–2729.

Highlights

- Ganglion cell directional tuning requires a high starburst cell dendritic density.
- Asymmetric wiring is preserved in direction selective circuits of *Sema6A*$^{-/-}$ mice.
- Sema6A$^{-/-}$ starburst cell varicosities maintain direction selectivity.
- Starburst cell dendritic tuning defined by distal excitatory input orientations.

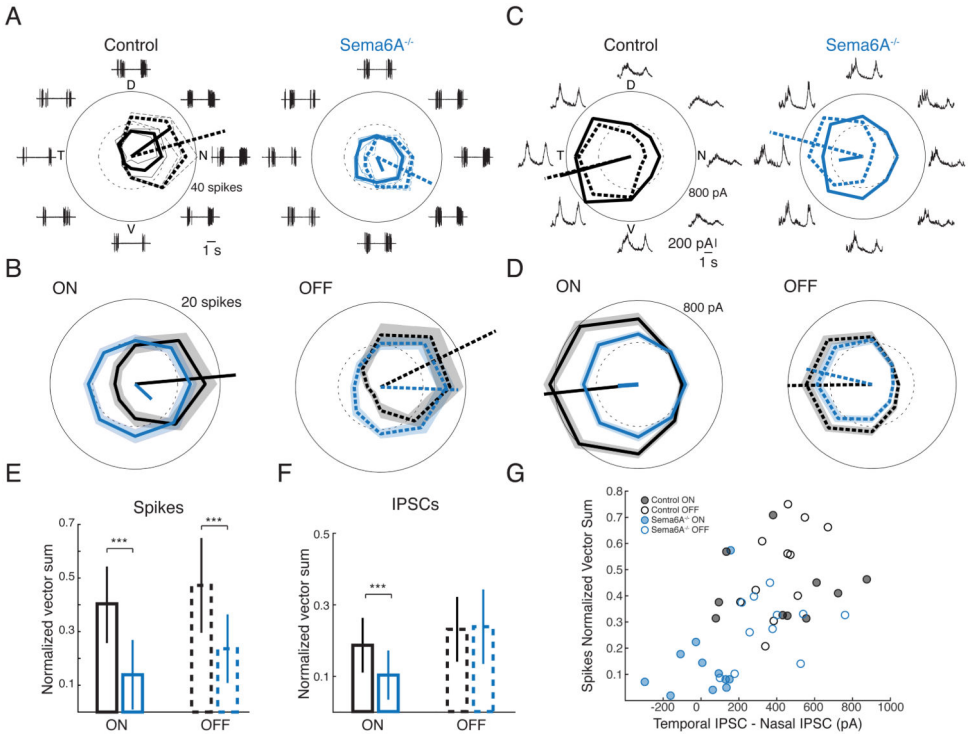

Figure 1. DSGCs in Sema6A$^{-/-}$ mice receive weak and symmetric inhibition

A. Example DSGC spikes to moving bars in eight directions. Tuning curves of mean spike counts for ON (solid) and OFF (dotted) responses are shown with respective vector sums. Thin lines are spike counts of individual trials. D, T, V,N = motion towards dorsal, temporal, ventral, or nasal retinal locations, respectively.

B. Average spike tuning curves across all DSGCs (n=13 littermate Controls, 17 Sema6A$^{-/-}$) ±sem.

C,D. Same as *A,B* for peak IPSCs. Individual trials were averaged before calculating peaks (n=15 Control, 21 Sema6A$^{-/-}$).

E,F. Normalized vector sums of tuning curves for ON and OFF responses ± sd. 1 way ANOVA, Tukey-Kramer post-hoc, $p < 0.001$.

G. Spike tuning increases with greater SAC-mediated inhibition for DSGC ON and OFF responses in both Control and *Sema6A*$^{-/-}$ mice.

See also Figure S1.

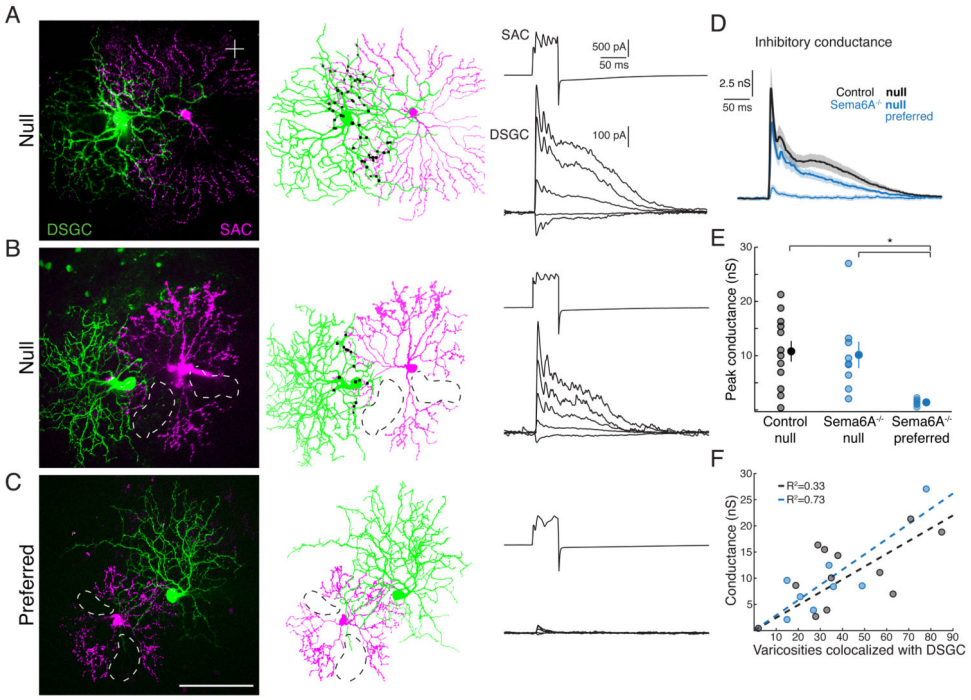

Figure 2. SAC-DSGC synaptic strength and asymmetric wiring is preserved in Sema6A$^{-/-}$mice

A-C. (left) Projections of 2-photon images, (middle) reconstructions with putative synaptic sites in black [9], and (right) inhibitory synaptic recordings from SAC-DSGC pairs. SAC capacitive transients are clipped. Dotted lines are missing portions of Sema6A$^{-/-}$ SAC dendritic arbors. D, T, V,N are retinal coordinates as in Figure 1.

D. Average inhibitory conductance traces ± sem for SAC-DSGC pairs. (n=12 Control, 9 Sema6A$^{-/-}$ null, 6 Sema6A$^{-/-}$ preferred).

E. Average peak inhibitory conductance ± sem. 1-way ANOVA $p < 0.0135$, Tukey-Kramer post-hoc, $p = 0.014$ Control vs Sema6A$^{-/-}$ preferred, $p = 0.032$ Sema6A$^{-/-}$ null vs preferred.

F. SAC-DSGC inhibitory conductance increases with the number of putative synaptic sites from null oriented SAC dendrites [9].

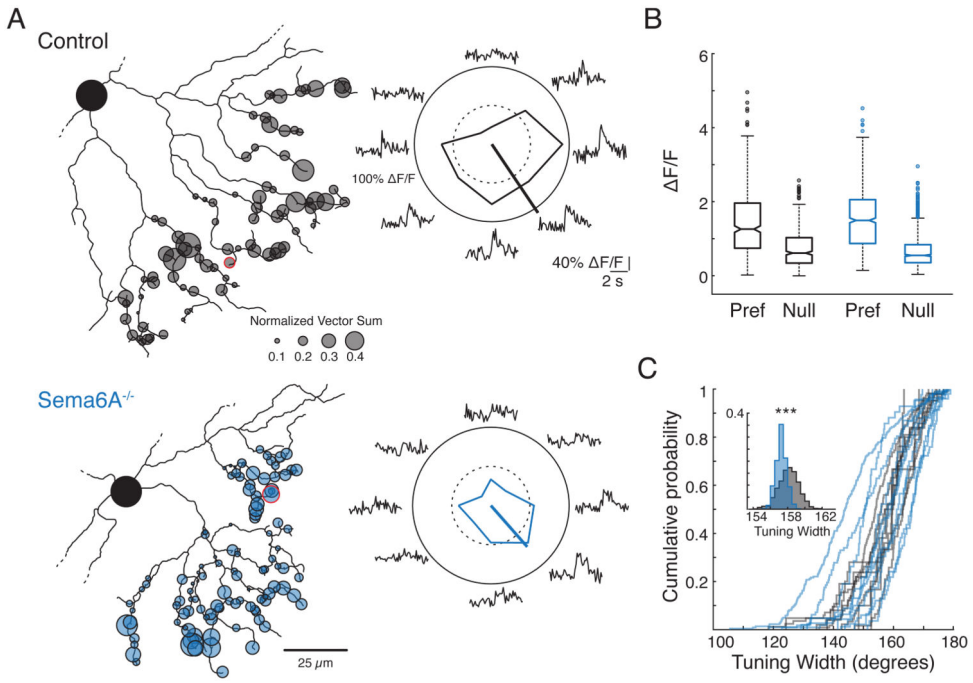

Figure 3. SAC varicosity DS is preserved in Sema6A$^{-/-}$ mice

A. (left) Reconstructions of Control (top) and Sema6A$^{-/-}$ (bottom) SACs with imaged varicosities denoted by semi-transparent circles. Circle diameter represents Ca^{2+} response tuning curve normalized vector sum magnitude, a measure of directional tuning. (right) Average Ca^{2+} responses (ΔF/Fo) and corresponding tuning curves of two example varicosities (red circles, left). The straight lines inside the polar plots indicate the vector sums.

B. Peak Ca^{2+} increases for Control or Sema6A$^{-/-}$ varicosities in response to stimulation along the preferred-null axis (n = 462 Control, 840 Sema6A$^{-/-}$ varicosities). Preferred responses are significantly different than null responses for both Control and Sema6A$^{-/-}$ SAC varicosities.Kruskal-Wallis, Tukey-Kramer post-hoc, $p < 0.001$.

C. Cumulative distributions for each SAC of varicosity Ca^{2+} response tuning widths. Inset: Probability distribution of mean tuning width for Control and Sema6A$^{-/-}$ varicosities after randomly sampling the same number of varicosities from each SAC. Sema6A$^{-/-}$ SAC varicosities have slightly smaller tuning widths, t-test $p < 0.001$.

See also Figure S2.

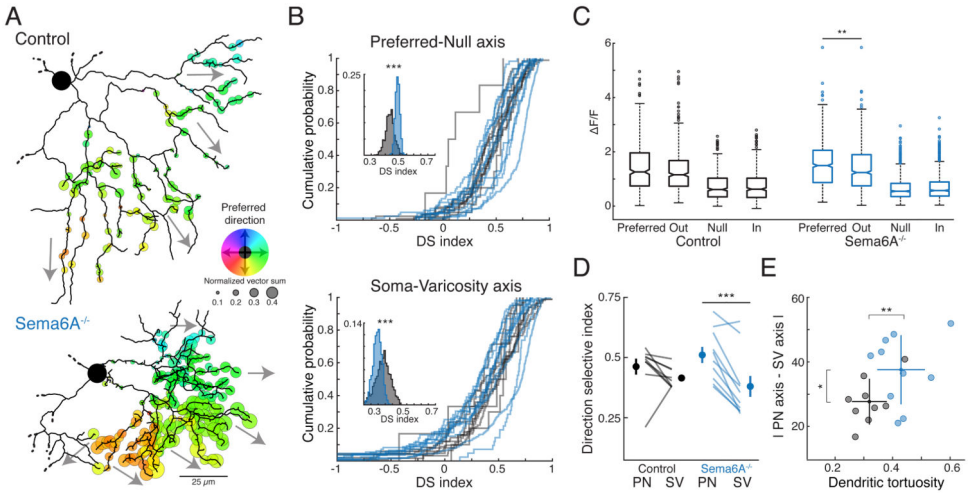

Figure 4. Sema6A$^{-/-}$ SAC varicosities are not necessarily tuned to centrifugal motion

A. Reconstructions of Control (top) and Sema6A$^{-/-}$ (bottom) SACs with imaged varicosities denoted by colored circles. Gray arrows indicate orientation of the proximal portion of the dendrite on which the surrounding varicosities are located. Inset: color code for varicosity preferred directions.

B. Cumulative distributions for each SAC (n = 9 Control, 10 Sema6A$^{-/-}$) of varicosity direction selectivity indices (see Methods) calculated along the preferred-null axis (top), defined by the orientation of the tuning curve vector sum for each varicosity, and along the soma-varicosity axis (bottom), defined by the anatomical angle from the SAC soma to each varicosity. Inset: Probability distribution of mean DS index for Control and Sema6A$^{-/-}$ varicosities after randomly sampling the same number of varicosities from each SAC. Sema6A$^{-/-}$ SAC varicosities have slightly higher DSIs along the preferred-null axis, t-test $p < 0.001$, and slightly lower DSIs along the soma varicosity axis, t-test $p < 0.001$.

C. Peak Ca^{2+} increases for Control (left) or Sema6A$^{-/-}$ (right) varicosities in response to different motion directions (n = 462 Control, 840 Sema6A$^{-/-}$ varicosities). Preferred and null are the responses along the preferred-null axis, and out and in are responses along the soma-varicosity axis. Sema6A$^{-/-}$ varicosities have a significant reduction in peak Ca^{2+} responses to outward motion compared to responses to preferred direction motion. All preferred and outward responses are significantly different than all null and inward responses, Kruskal-Wallis, Dunn-Sidák post-hoc, $p < 0.001$, ** $p = 0.0016$.

D. Average varicosity direction selective index (see Methods) for each imaged SAC. Indices were calculated using Ca^{2+} responses along the preferred-null axis (PN) or along the soma-varicosity axis (SV). Paired t-test, $p = 0.17$ Control, $p < 0.001$ Sema6A$^{-/-}$.

E. Average absolute angular difference between the preferred-null axis and the soma-varicosity axis for the varicosities on each SAC as a function of average dendritic tortuosity (see Methods). t-test, $p = 0.032$ angular difference, $p = 0.005$ tortuosity.

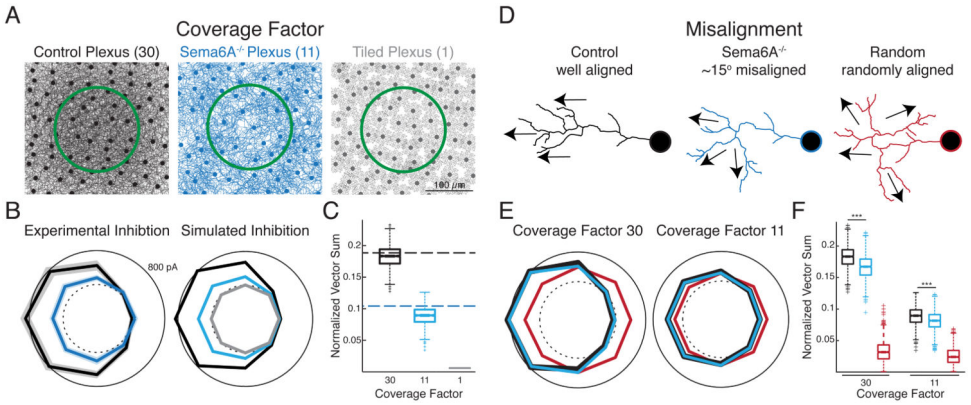

Figure 5. Reduced SAC dendritic coverage in *Sema6A*$^{-/-}$ mice leads to weak and symmetric inhibition in DSGCs

A. Schematic depicting differences in the SAC coverage factor between Control retinas, Sema6A$^{-/-}$ retinas, and retinas with a SAC coverage factor of 1. Green circle indicates extent of DSGC dendritic arbor. The shorter dendrites in Sema6A$^{-/-}$ SACs leads to a 63% reduction in dendritic coverage (see [17]).

B. (left) Average ON response IPSC tuning curves ± sem for DSGCs in Control (black) and Sema6A$^{-/-}$ (blue) mice in response to moving bar stimulation (see Figure 1D). Accounting for the symmetric inhibitory contribution from non-SAC GABAergic amacrine cells [19, 20], there is a 67% reduction in SAC-mediated inhibition for DSGCs in Sema6A$^{-/-}$ mice compared to Control. (right) Simulated IPSC tuning curves for DSGCs based on SAC coverage factors in Control (black), Sema6A$^{-/-}$ (blue), and coverage factor 1 (grey) conditions.

C. Normalized vector sum magnitudes for IPSC tuning curves from experimental (dotted lines) and simulated (boxplots) data in B. The simulated inhibition based on the Sema6A$^{-/-}$ SAC coverage factor leads to a reduction in overall IPSC directional tuning matching the experimental data.

D. Schematic depicting alignment between soma-varicosity angles and varicosity preferred directions used in the simulation in E,F (see Figure 4).

E. Simulated IPSC tuning curves for DSGCs at Control (30) and Sema6A$^{-/-}$ (11) SAC coverage factors in which angular differences between SAC varicosity anatomical and functional axes were randomly drawn from the experimental Control (black) and Sema6A$^{-/-}$ (blue) data (Figure 4E). The same simulation was also performed using randomly drawn differences between anatomical and functional axes from -359 to 359 degrees (red).

F. Normalized vector sum magnitudes for IPSC tuning curves from simulated data in E. The misalignment between the SAC-DSGC wiring axis and varicosity preferred directions in *Sema6A*$^{-/-}$ mice leads to a significant reduction in IPSC tuning, with larger reductions occurring at denser SAC coverages. DSGCs would experience symmetric inhibitory input with a complete loss of alignment in more tortuous SAC dendrites (red). Kruskal-Wallis, Tukey-Kramer post-hoc,*** $p < 0.001$.

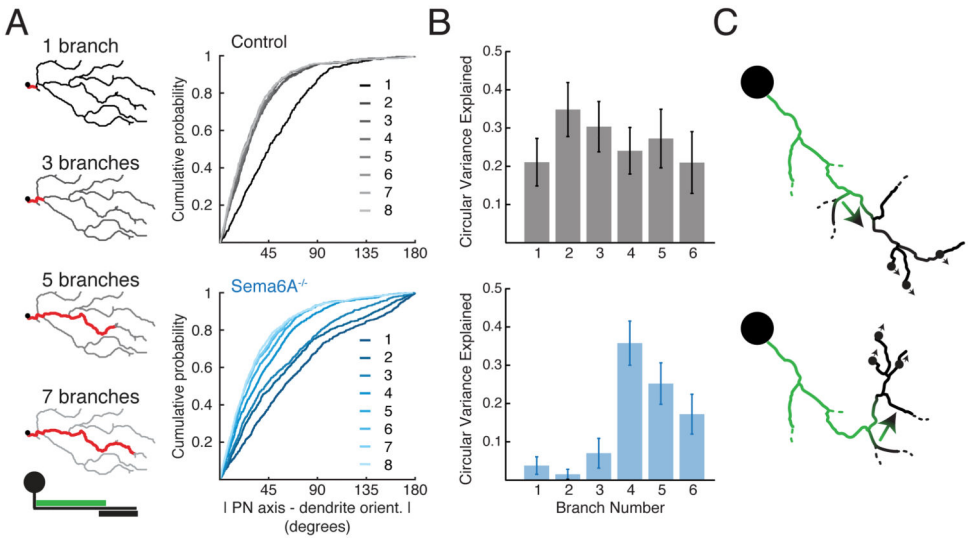

Figure 6. Varicosity preferred directions are determined by the angle of the SAC dendrite at the end of the bipolar cell input distribution

A. (left) Schematics showing the portion of the dendrite used for determining average dendritic orientation. (bottom) Schematic depicting average location of glutamatergic inputs (green) and release sites (black) on a SAC process [1, 5]. (right) Cumulative distributions of absolute angular differences between the orientation of Ca^{2+} response tuning curve vector sums for each varicosity and the average orientations of portions of the dendrite on which the varicosity is located. Lighter lines indicate angular differences computed using dendritic orientations of portions of the SAC dendrite farther from the soma as indicated by the legend (n = 462 Control varicosities, 840 $Sema6A^{-/-}$ varicosities).

B. Bootstrapped circular regression analysis shows that the variance in varicosity preferred directions is best explained by the angle of the 4^{th} branch order SAC dendritic segment. Error bars are 95% confidence intervals.

C. Schematic depicting Control (top) and $Sema6A^{-/-}$ (bottom) SACs. Varicosity (black circle) preferred directions are determined by the angle of the SAC dendrite at the end of the bipolar cell input distribution (green).

See also Figure S3.